Materials Horizons

ROYAL SOCIETY OF CHEMISTRY

COMMUNICATION

View Article Online
View Journal

Cite this: DOI: 10.1039/d0mh00131g

Received 23rd January 2020,
Accepted 8th June 2020

DOI: 10.1039/d0mh00131g

rsc.li/materials-horizons

Bone-inspired healing of 3D-printed porous ceramics†

An Xin,[a] Kunhao Yu,[a] Runrun Zhang,[a] Bingyuan Ruan,[a] Allyson L. McGaughey,[a] Zhangzhengrong Feng,[a] Kyung Hoon Lee,[a] Yong Chen,[b] Amy E. Childress[a] and Qiming Wang *[a]

Emerging 3D-printed ceramics, though showing unprecedented application potential, are typically vulnerable to fractures and unable to heal at room temperature. By contrast, their natural counterparts, human bones, exhibit extraordinary self-healing capability through the activation of stem cell osteoblasts that precipitate mineralized calluses to enable interfacial healing at body temperature. Inspired by bones, we here employ bacteria as artificial osteoblasts to enable healing of 3D-printed porous ceramics at room temperature. The healing behavior relies on bacteria-initiated precipitation of calcium carbonate crystals to bridge fracture interfaces of ceramics. We show that bacteria-loaded porous ceramics can heal fracture interfaces to restore 100% mechanical strength at room temperature, and the healed strength is not compromised by heating up to 500 C or by corrosion of alkalis and oxidants. The bacteria-assisted healing mechanism is revealed by systematic control experiments, and the healing strength is explained by cohesive fracture modeling. We further incorporate this method into 3D-printed ceramics and demonstrate on-demand healing of ceramic dental crowns, ceramic water membranes, and ceramic lattices, and autonomous healing of ceramic armor. As the first-generation healing mechanism of 3D-printed ceramics, this paradigm is expected to open promising avenues for revolutionizing the low-damage-tolerance nature of existing 3D-printed ceramics.

New concepts

We demonstrate a new paradigm in harnessing bacteria to enable on-demand and autonomous healing of 3D-printed ceramics. Improving the damage tolerance of 3D-printed ceramics has been a long-lasting endeavor. Most of the existing efforts have been devoted to improving the fracture resistance of the constituent materials; however, healing of the damaged 3D-printed ceramics remains largely unexplored. The concept proposed in this paper fills this technology gap by using carbonate-precipitating bacteria to heal 3D-printed ceramics. Bacteria-assisted healing of 3D-printed ceramics at room temperature may facilitate *in situ* or autonomous healing of ceramics with various complex architectures for a wide range of applications, such as *in vitro* biomedical devices, water treatment membranes, lattice structures, and body armor.

Introduction

Emerging additive manufacturing technologies for ceramics[1–7] have exhibited encouraging promise in a wide range of engineering applications, such as machine engines,[8] energy storage devices,[9] biomedical devices,[10] water membranes,[11] and body armor.[12] Despite the promise, a long-standing challenge is that 3D-printed ceramics typically feature low tolerance to damages and fractures.[1–7] Most of the existing strategies to improve the damage tolerance of 3D-printed ceramics have been relying on reinforcing the ceramics with nanomaterials[13] or minimizing defects.[3] However, healing fractures of 3D-printed ceramics has not been demonstrated to date. Existing healable bulk ceramics primarily rely on oxidation or re-sintering at high temperatures (>1000 °C).[14–21] The high-temperature requirement precludes any *in situ* or autonomous healing of ceramics that operate at low temperatures, such as *in vitro* biomedical devices,[10] water membranes,[11] and body armor.[12] Therefore, development of a paradigm to enable healing of 3D-printed ceramics at low temperatures (*e.g.*, room temperature), while showing promising application potential, is still an outstanding challenge.

On the other hand, this challenge has already been addressed by 3D-architected human bones that show extraordinary healing capability at body temperature (37 °C). The healing of a fractured human bone relies on stem cells called osteoblasts to precipitate mineralized calluses (primarily $Ca_{10}(PO_4)_6(OH)_2$) to bridge fracture interfaces (Fig. 1A).[22–24] The healing process starts from hematoma formation around the fracture location. Then, osteoblasts within the hematoma initiate precipitation of calluses that remodel to hard calluses and spongy bones to bridge the

[a] Sonny Astani Department of Civil and Environmental Engineering, University of Southern California, Los Angeles, CA 90089, USA. E-mail: qimingw@usc.edu
[b] Epstein Department of Industrial and Systems Engineering, University of Southern California, Los Angeles, CA 90089, USA

† Electronic supplementary information (ESI) available. See DOI: 10.1039/d0mh00131g

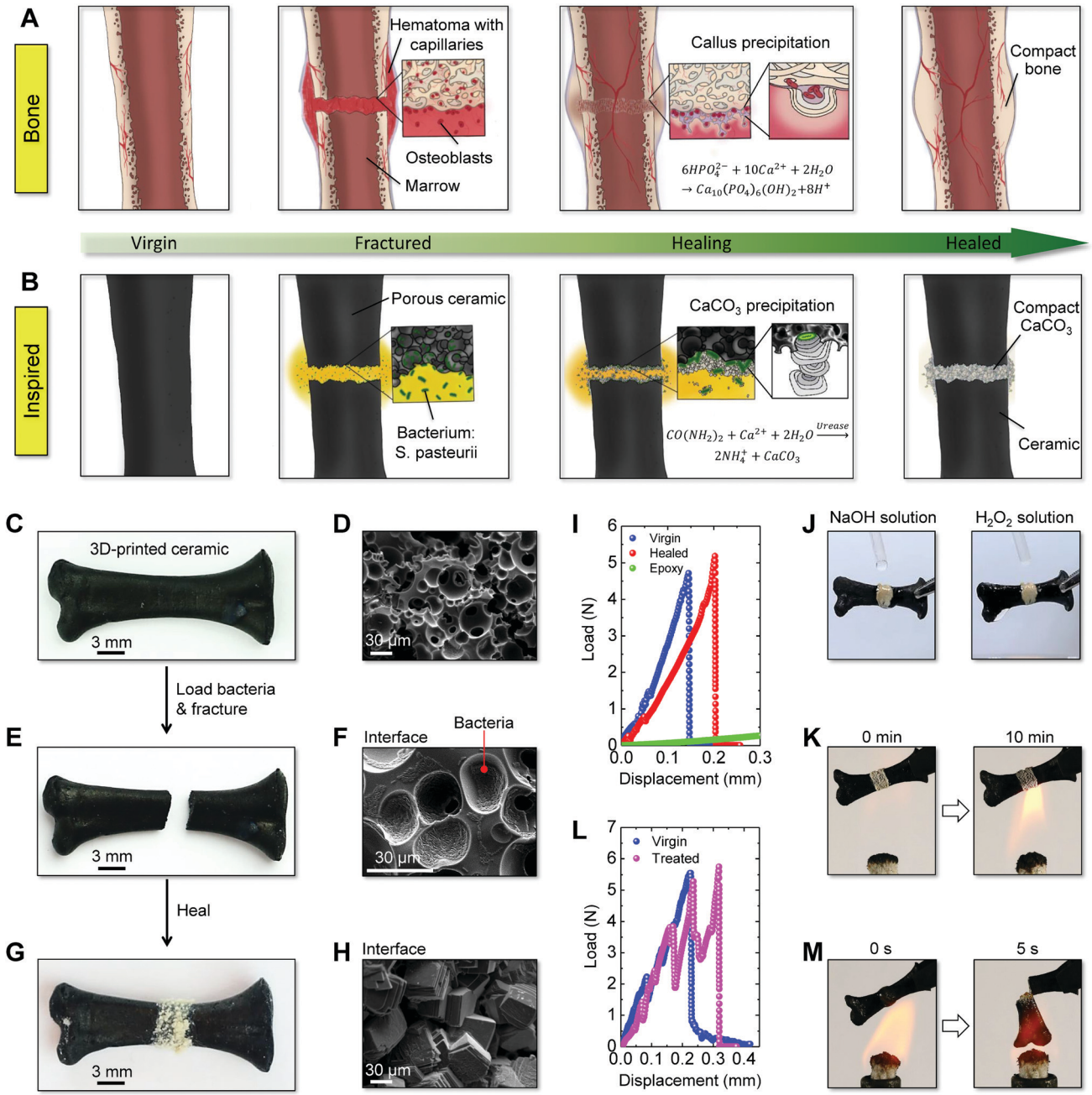

Fig. 1 Bioinspired healing of ceramic bones. (A) Schematics for the healing process of a fractured human bone enabled by osteoblast-induced precipitation of callus. (B) Schematics for the healing process of a fractured ceramic bone enabled by bacteria-assisted precipitation of $CaCO_3$. (C) 3D-printed ceramic bone sample. (D) Scanning electronic microscope (SEM) image of the microstructure of ceramic bone. (E) Broken ceramic bone. (F) SEM image of the interface of the broken ceramic bone with attached bacteria. (G) Healed ceramic bone with $CaCO_3$ crystals bonded on the fracture interface. (H) SEM image of the healing interface of the healed ceramic bone. (I) Load–displacement curves of virgin and healed ceramic bones in three-point-bending tests. (J) Healed ceramic bones with NaOH solution (4.8 mol L^{-1}) and H_2O_2 solution (8.8 mol L^{-1}) dropped onto the healed interface, respectively. (K) The ceramic bone healed by interfacial $CaCO_3$ precipitation before and after exposure to a lamp fire (650–750 °C) for 10 min. The lamp is fueled by a mixture of 70% ethanol and 30% water. (L) Load–displacement curves of a virgin bone and a healed bone after corrosion treatment of NaOH solution (4.8 mol L^{-1}) and H_2O_2 solution (8.8 mol L^{-1}) and annealing up to 500 °C for 30 min. (M) Ceramic bone repaired by a commercial epoxy glue before and after exposure to the lamp fire for 5 s.

fracture interface. Eventually, the spongy bones transform into compact bones to fully repair the fracture interface. This paradigm applies to any bone geometries given that osteoblasts and necessary ingredients can be delivered to the fracture location. This natural paradigm, if successfully implemented in engineering materials, would greatly benefit and advance various fields of traditionally unhealable stiff materials such as ceramics. Despite the potential, encapsulation and activation

Table 1 Comparison between healing of human bones and bacteria-assisted healing of 3D-printed ceramics

Comparison items	Healing of bones	Healing of 3D-printed ceramics
Porosity of virgin material	70–85%[31]	40–80%
Young's modulus of virgin material	100–500 MPa (cancellous bone)[32–34]	100–300 MPa
Shape of virgin structure	3D-architected	3D-architected
Fracture interface	Curved	Curved
Healing initiator	Osteoblast	Bacterium
Precipitated substance	Callus (primarily $Ca_{10}(PO_4)_6(OH)_2$)	$CaCO_3$
Healing time	1–4 months[35]	6–12 days

of living osteoblasts within engineering materials are challenging tasks.[25]

Inspired by the healing of bones, we here employ bacteria as artificial osteoblasts to enable interfacial healing of 3D-printed ceramics at room temperature (Fig. 1A and B, the comparison shown in Table 1). Although bacteria-assisted healing has been applied to cementitious materials,[26–30] it remains elusive how to employ bacteria to heal 3D-printed ceramics. The healing paradigm relies on bacteria-initiated precipitation of mineralized calcium carbonates ($CaCO_3$) to bridge fracture interfaces of porous ceramics.[28,29] The key mechanism of healing is that the bacteria-initiated precipitation of $CaCO_3$ on the fracture interface leads to a strong interfacial bonding with the ceramic surface. Harnessing this mechanism, we demonstrate 100% strength restoring of fractured ceramics within days (6–12 days for different conditions) at room temperature. Despite forming at room temperature, the healed interface can sustain temperatures as high as 500 °C, as well as the corrosion of alkali and oxidants, without compromising the healing strength. The healing mechanism is verified by control experiments, and the healing strength is explained by cohesive fracture simulations. We then apply this paradigm to 3D-printed ceramics to demonstrate on-demand healing of ceramic dental crowns, ceramic water membranes, and ceramic lattice structures, and autonomous healing of ceramic armor. As the first-generation healing mechanism of 3D-printed ceramics, the proposed paradigm is expected to open promising avenues for revolutionizing the low-damage-tolerance nature of 3D-printed ceramics that are used in a wide range of applications, such as *in vitro* biomedical devices, separation membranes, body armor, and lightweight structures.

Results and discussion

Bacteria-assisted healing of porous ceramics

To demonstrate the overall process of the proposed paradigm, we take a 3D-printed bone-like ceramic as an example (Fig. 1C). We first employ a stereolithography-based additive manufacturing system to fabricate a poly(methyl methacrylate) (PMMA) microparticle-filled preceramic polymer in a bone shape (mean PMMA particle size 48 μm, Fig. S1 and S2, ESI†). We then sinter the polymer structure to form a porous SiOC ceramic structure with a mean pore size of ~28 μm (Fig. 1C, D and Fig. S3, S4, ESI†). The pores are openly interconnected, making the material permeable to water. We then immerse the porous bone into a medium containing urease-producing bacteria *S. pasteurii* for 24 h to enable the bacteria to attach to the pore surfaces.[36] The presence of bacteria on the pore surface is verified by interfacial scanning electron microscope (SEM) images of the broken sample (Fig. 1E and F). Note that the bacteria still attach well to the ceramic surface after several cycles of water flushing. Subsequently, we contact two broken bone pieces (Fig. 1E), fasten their relative positions with a gap of ~300 μm, and allow the fracture interface to contact a precipitation medium with urea and Ca^{2+} (Fig. S5, ESI†). After 10 days, crystals nucleate on the interface and firmly bridge the fractured interface (Fig. 1G). Energy dispersive X-ray microanalyses confirm that the crystals are $CaCO_3$ (Fig. S6, ESI†). SEM images show that $CaCO_3$ crystals cover the whole fractured interface (Fig. 1H). Note that VHB tapes are used to cover other regions and leave the region around the fracture interface open to the precipitation medium (Fig. S5, ESI†); thus, only the region around the fracture interface shows the accumulation of white crystals (Fig. 1G).

To quantify the healing performance, we employ three-point-bending (3PB) to apply loads to the virgin and healed samples around the healing interfaces (Fig. S7, ESI†). We find that the maximal load of the healed ceramic bone after a 10-day healing period is approximately 105% of that of the virgin sample (Fig. 1I). Besides, the healed interface can safely sustain corrosion of a strong alkali solution (4.8 mol L^{-1} NaOH) and a strong oxidant solution (8.8 mol L^{-1}, H_2O_2) (Fig. 1J and Movie S1, ESI†). Since the formed $CaCO_3$ crystals can be dissolved by acids, the proposed method is not applicable to acidic conditions. Despite forming at room temperature, the healed interface can sustain an active fire with a temperature of 650–750 °C for over 10 min without loss of integrity (Fig. 1K and Fig. S8, Movie S2, ESI†). To quantify the effect of the corrosion and heat treatments on the healed sample, we first rinse the sample in NaOH solution (4.8 mol L^{-1}) and H_2O_2 solution (8.8 mol L^{-1}), and then anneal the ceramic bone by gradually increasing the temperature to 500 °C and maintaining at 500 °C for half an hour (Fig. S9, ESI†). We find that the sample still exhibits 103% strength of the virgin sample in the 3PB test (Fig. 1L). In contrast, ceramic samples repaired by a commercial epoxy glue (Gorilla glue) show three drawbacks (Table S1, ESI†): (1) the maximal load of an epoxy-repaired ceramic sample is only 10% of that of the virgin sample (Fig. 1I). (2) Epoxy typically exhibits significant aging in the alkaline or oxidative environment.[37,38] (3) An epoxy-repaired ceramic sample immediately breaks into two parts if it is mounted over an active fire (650–750 °C, Fig. 1M).

Characterization of healing evolution

To characterize the healing evolution, we carry out healing experiments of rectangular porous ceramic plates over 14 days (Fig. 2). During the healing process, the precipitated $CaCO_3$ crystals are expected to gradually grow and eventually bridge the fracture interface (Fig. 2A). Optically, more and more white crystals precipitate around the fractured interface with increasing healing days (Fig. 2B). The crystal growth is confirmed by SEM images of the healing interfaces: both size and surface coverage of the adhered crystal particles increase with increasing healing

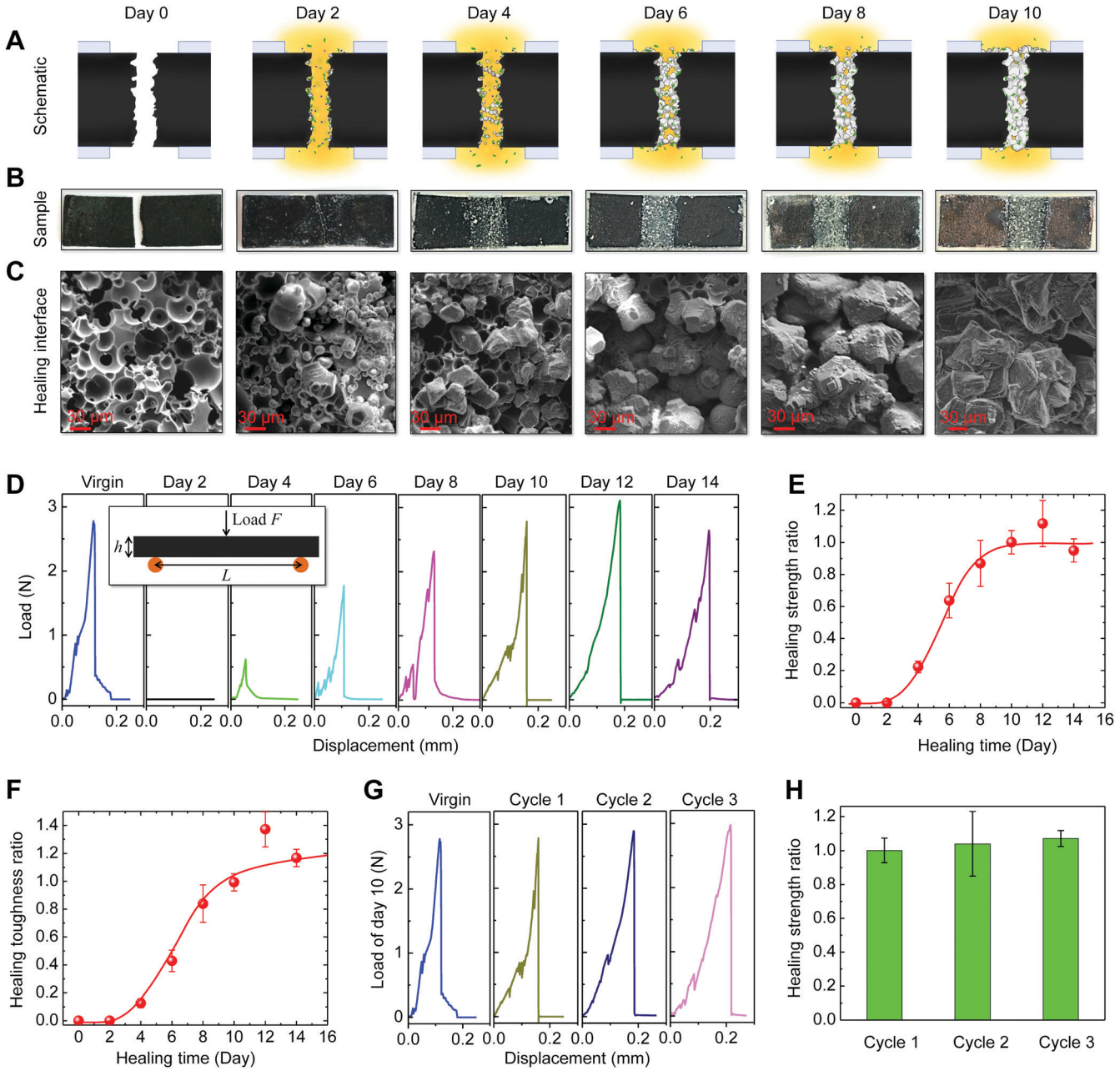

Fig. 2 Characterization of bacteria-assisted healing evolution. (A) Schematics of nucleation and growth of bacteria-assisted precipitation of $CaCO_3$ crystals on the fracture interface over 10 days. (B) Healing of ceramic plate samples (length 17 mm, width 5.68 mm, and thickness 1.42 mm) over 10 days. (C) SEM images of healing interfaces of ceramic plate samples over 10 days. (D) Load–displacement curves of virgin and healed samples over 10 days in 3PB tests. The inset shows the schematic for the 3PB test, where F is the applied load, L is span between two supporting points, and h is sample thickness. Flexural strength is calculated as $(3F_mL)/(2bh^2)$, where F_m is maximal load and b is sample width. (E) Healing strength ratios of ceramic plates as a function of healing time. Healing strength ratio is defined as the effective flexural strength of healed samples normalized by that of the virgin sample. (F) Toughness ratios of ceramic plates as a function of healing time. Toughness is defined as the enclosed area of the load–displacement curve shown in (D). Toughness ratio is defined as toughness of healed samples normalized by that of the virgin sample. (G) Load–displacement curves of virgin and healed samples after 10 days for three healing cycles. (H) Healing strength ratios of healed samples after 10 days for three healing cycles. Error bars in (E), (F), and (H) represent standard deviations for 3–5 samples.

days (Fig. 2C and Fig. S10, ESI†). When the healed sample is broken into two parts, $CaCO_3$ crystals can be found on both fracture interfaces (Fig. S11, ESI†), implying that the bonding strength between the $CaCO_3$ crystals and the ceramic surface is stronger than the cohesive strength of the $CaCO_3$ crystals. The healing strengths of the virgin and healed ceramics are further characterized by 3PB tests (Fig. 2D). The Young's modulus and flexural strength of the virgin porous ceramic (porosity 56.4%) are measured as ~175 MPa (Fig. S4D, ESI†) and 345 kPa (Fig. 2D). We find that the maximal loads of the 3PB tests increase with increasing healing days until reaching a plateau that is around the maximal load of the virgin ceramic. We then calculate the effective flexural strength of the healed interface and normalize it with virgin flexural strength to obtain the healing strength ratio. We find that the healing strength ratio increases with the healing time and reaches a plateau around 100% after 10 days (Fig. 2E). The toughness of the healed sample (enclosed area of the load–displacement curve) also increases with the healing days and then reaches a plateau at 100–120% of the virgin toughness (Fig. 2F). Interestingly, the healing process shown is repeatable (Fig. 2G). We repeat healing experiments after re-breaking the healed interface for three sequential cycles, and find that the healing strength of day 10 remains approximately 100% over three healing cycles (Fig. 2G and H).

Examination of healing mechanism

Based on the characteristics of the healing evolution, the healing process is hypothesized as follows: after exposure to the bacteria-containing medium, bacteria *S. pasteurii* grow within the porous ceramic and attach to the pore surface (Fig. 3A(i)). Once the ceramic is fractured and adequate precipitation chemicals (*e.g.*, urea and Ca^{2+}) are delivered to the fracture location, bacteria produce an enzyme called urease which decomposes urea to initiate the nucleation of $CaCO_3$ crystals around the bacteria (Fig. 3A(ii) and Fig. S12, Materials and methods).[28,29] Then crystals gradually grow to cover the bacteria and bond on the ceramic surface (Fig. 3A(iii)). The crystals then grow into larger particles (Fig. 3A(iv)), and new crystals nucleate and grow on the existing crystal particles (Fig. 3A(v)), eventually bridging the fracture interface.

According to the hypothesized mechanism, the key to interfacial healing is the bacteria-initiated interfacial nucleation of $CaCO_3$, which leads to strong bonding between the $CaCO_3$ crystal and the ceramic (Fig. 3A(ii) and (iii)). To validate this mechanism, we carry out three control experiments (Fig. 3B): (1) control 1: only bacteria are provided, without precipitation chemicals (urea and Ca^{2+}); (2) control 2: only precipitation chemicals are provided, without bacteria; and (3) control 3: the precipitation chemicals in control 2 are replaced by $CaCl_2$ and Na_2CO_3 which are expected to enable strong chemical reaction to form $CaCO_3$ through a homogeneous nucleation process, without bacteria. The results show that the interfacial strengths of these three controls are either zero or much smaller than that of the experimental case (Fig. 3B and Fig. S13, ESI†). Their interfacial precipitations are also much less than that of the experimental case (Fig. 3B(i)–(iv)). In control 1, no precipitation is observed over 10 days, as expected because no precipitation chemicals are provided (Fig. 3B(ii)). In control 2, a smaller fraction of precipitation is observed relative to the experimental case, because no bacteria serve as the precipitation initiators (Fig. 3B(iii)). In control 3, crystal particles with small sizes (<10 μm) are observed on the interface (Fig. 3B(iv)). These particles are fundamentally different from the ones formed *via* heterogeneous interfacial nucleation on the ceramic surface (Fig. 3B(i)),[39] because they are isolated particles formed through a homogeneous nucleation process and show little or even no bonding with the ceramic surface. Thus, the interfacial strength of control 3 is almost zero (Fig. 3B). These control tests imply that the strong interfacial bonding requires bacteria to initiate the heterogeneous interfacial nucleation of crystals on the ceramic surface.

Then, we develop a theoretical model for crystal particle growth during the process shown in Fig. 3A(ii)–(iv) (Section 1 of ESI† and Fig. S14). The model harnesses the mass balance between the consumed solute $CaCO_3$ during the precipitation process and transferred solute $CaCO_3$ through diffusion around a semi-spherical nucleus.[39,40] The model shows that the crystal particle size d grows following a scaling law $d \propto \sqrt{t}$, where t is healing time during the growth process of a single particle. The scaling law is roughly verified with the experimentally measured particle size on the healing interface from 0 to 8 days (Fig. S10A, ESI†).

Third, we further develop cohesive-zone models to simulate fracture behaviors of healed ceramics under 3PB loads (Fig. 3C–E and Fig. S15, ESI†). Based on the hypothesized bonding mechanism, we model the interfacial bridges using cohesive zone elements with bilinear traction–separation laws in finite element models (Fig. S15B and Table S2, ESI†). We hypothesize that the stiffness and strength of the cohesive zone elements increase as the healing time increases, because the area concentration of the $CaCO_3$ crystal bridge increases during the healing process. Using measured stiffnesses and estimated interfacial strengths of the cohesive zone (Table S2, ESI†), we can simulate the fracture processes and obtain corresponding load–displacement relations of 3PB tests for healed interfaces of various strengths (Fig. 3C–F and Movies S3–S5, Table S2, ESI†). We find that the maximal loads coincide with the fracture initiation on the healed interfaces because samples primarily show brittle failures (Fig. 3F). The simulated maximal loads consistently match with experimental results for healing days 4–10 (Fig. 3F and G).

Effect of medium and material on healing performance

Next, we study the effects of various medium/material parameters on the healing performance (Fig. 3H–J). First, the availability of Ca^{2+} significantly affects the precipitation rate on the healing interface. As we decrease the concentration of Ca^{2+} within the precipitation medium, the size and area coverage of crystals decrease (Fig. 3H(i)–(iii)), and the healing strength ratio for day 10 decreases accordingly (Fig. 3H and Fig. S16, ESI†). Second, the pore size of the porous ceramic also affects the healing performance (Fig. 3I and Fig. S17A, ESI†). For porous ceramic samples with a mean pore size of ~3.5 μm, very few crystals precipitate on the healing interface (Fig. 3I(i)), because the

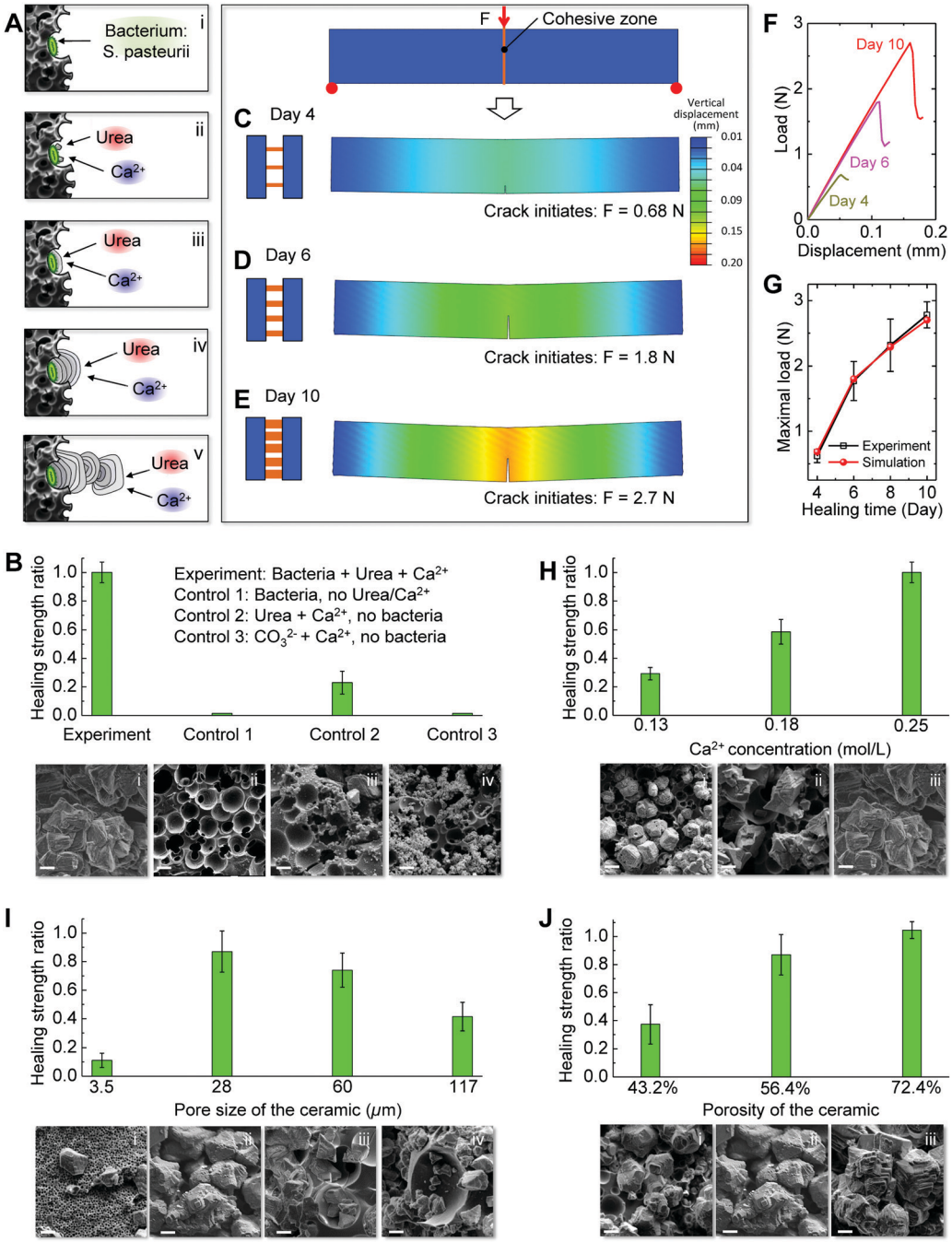

Fig. 3 Mechanism of bacteria-assisted healing of porous ceramics. (A) Schematics to show bacteria-assisted nucleation and growth of $CaCO_3$ crystals on a ceramic surface. (B) Healing strength ratios on day 10 of the experimental case (bacteria with precipitation medium), control 1 (no precipitation medium), control 2 (no bacteria), and control 3 (homogeneous nucleation of $CaCO_3$). The corresponding SEM images of the healing interfaces are shown in (i–iv). (C–E) Schematics to show $CaCO_3$-bridged three healed interfaces and finite element simulations to show fracture initiations on three healed interfaces. The small crystal particles on (3B(iv)) are formed *via* homogeneous nucleation and show little or even no bonding with the ceramic surface. (F) Simulated loads as functions of displacements of 3PB tests for three different healed interfaces: day 4, 6, and 10. (G) Comparison of numerically simulated and experimentally measured maximal loads in 3PB tests for healing days 4–10. The experimentally measured maximal loads are obtained from Fig. 2D. (H) Healing strength ratios on day 10 and corresponding interfacial SEM images (i–iii) of the ceramic samples with various Ca^{2+} concentrations (0.13 mol L^{-1}, 0.18 mol L^{-1}, and 0.25 mol L^{-1}). (I) Healing strength ratios on day 8 and corresponding interfacial SEM images (i–iv) of the ceramic samples with various pore sizes. The mean pore sizes 3.5, 28, 60, and 117 μm correspond to PMMA particle mean sizes 6, 48, 100, and 200 μm, respectively. (J) Healing strength ratio on day 8 and the corresponding interfacial SEM images (i–iii) of the ceramic samples with various porosities (43.2, 56.4, and 72.4%). Scale bars in (B) and (H–J) represent 30 μm. Error bars in (B), (G), and (H–J) represent standard deviations for 3–5 samples.

bacteria with a size of 3–7 μm may not be able to enter the pore and proliferate within the pore (Fig. S17B, ESI†). As the pore size increases, the bacteria are expected to proliferate better within the porous ceramic and enable more $CaCO_3$ precipitations (Fig. 3I(ii)–(iv) and Fig. S17C, ESI†). However, as the pore size becomes much larger than bacterial size, it becomes challenging for the bacteria to precipitate crystals to cover the ceramic pores (verified by the SEM image of Fig. 3I(iv)), which may lead to a relatively low interfacial bonding (Fig. S17D and E, ESI†). Therefore, as pore size increases, the healing strength ratio first increases and then decreases, with a maximum when the pore size is 4–8 times the bacterial size (*e.g.*, 28 μm pore size, Fig. 3I). Third, the healing performance of the ceramic samples is affected by the ceramic porosity (Fig. 3J). For example, when the porosity of the ceramic increases from 43.2 to 72.4% with a mean pore size of 28 μm, the healing strength ratio increases accordingly (Fig. 3J and Fig. S18, ESI†), likely because more bacteria can grow within the ceramic pores. As porosity increases (corresponding to increasing particle concentration), 3D-printing becomes more challenging;[41] to balance the healing performance and manufacturability, we select ceramics with 56.4% porosity for the 3D-printing in the following experiments.

Healing of 3D-printed ceramic structures

On-demand healing of ceramic dental crown. As the first example, we show the paradigm can be used to heal ceramic dental crowns. A dental crown is a prosthetic cap that covers a damaged tooth and protects the underlying gum. The most widely used dental crown is made of ceramics because ceramics can sustain corrosion by biological liquids.[42] Due to property mismatch between ceramic crowns and real teeth, dental crowns may fracture during force-sustaining service. However, existing ceramic dental crowns are typically expensive, mostly due to the degree of customization needed in the tooth repair.[42] Here we propose bacteria-induced healing of dental crowns. To demonstrate the concept, we 3D-print a ceramic dental crown and break it into two parts by applying a compressive load *via* a transverse rod (Fig. 4A and B). Then, we apply a bacterial medium with non-infectious *S. pasteurii* and corresponding precipitation medium around the fractured interface to enable $CaCO_3$-precipitation-induced healing over 10 days (see Materials and methods). The rod-compression test on the healed sample shows that the maximal compressive load is almost 90% that of the virgin ceramic crown (Fig. 4C). Note that the employed healing bacteria can be killed after the healing process, and thus would not affect the usage in the oral cavity.

On-demand healing of ceramic water membranes. As the second example, we show bacteria-induced healing of ceramic water treatment membranes in flat-sheet and tubular shapes. We 3D-print porous ceramic water membrane sheets and tubes (pore size 28 μm, porosity 56.4%) (Fig. 4D). These membranes can be used to filter suspended solids of wastewater (Fig. 4E). If the membrane is broken, filtrate water quality becomes poor because particles can flow through the interfacial crack (Fig. 4E). After the crack is healed by the bacteria-induced crystal precipitation, the filtrate water becomes clear again (Fig. 4E). To quantify filtration performance, we measure the hydraulic permeability of the virgin, broken and healed membranes (Fig. S19, ESI†). The hydraulic permeability of the virgin membrane is 3.9×10^{-13} m^2 (Fig. 4F). After being broken, the hydraulic permeability increases 34 times to 1.3×10^{-11} m^2 due to the loss of integrity (Fig. 4F). After the crack is healed, the permeability around the healing interface decreases to 5.5×10^{-13} m^2, which is slightly higher than the permeability of the virgin membrane (Fig. 4F). The higher permeability of the healed region is probably because the porosity of the precipitated $CaCO_3$ crystals around the healed interface is higher than the porosity of the virgin ceramic.

On-demand healing of ceramic lattice structures. In the third example, the healing paradigm is applied to ceramic lattice structures. Ceramic lattices emerge as promising lightweight structures due to their low density, high specific stiffness and strength, and high corrosion resistance.[3–7,43,44] However, fractured ceramic lattice structures may immediately lose properties and functions. Healable ceramic lattice structures have not been reported to date. To demonstrate the concept, we fabricate ceramic trusses that features two-order hierarchical pores with the first-order pores of a mean size of 28 μm within the truss beam and the second-order pores being ~1 mm within the truss voids, resulting in a very low relative density ρ/ρ_0 = 7% (Fig. 4G).[7,43] Using a 3PB tests (Fig. 4G and H), we measure effective stiffness (Fig. 4I) and flexural strength (Fig. 4J) of the virgin truss as 2.9 MPa and 0.14 MPa, respectively. After being broken, the fractured ceramic truss cannot sustain the bending load anymore. When bacteria and precipitation medium are applied around the fracture interface for 10 days, $CaCO_3$ crystals heal the interface and restore the stiffness and strength of the ceramic truss to 2.1 MPa and 0.16 MPa, respectively, though the relative density increases to ρ/ρ_0 = 10.6% due to the attachment of crystals around the healing interface (Fig. 4G). This healing mechanism is then tested for lattices with various relative densities between 5% and 10% (Fig. 4I, J and Fig. S20, ESI†). The scaling laws of the stiffness-density and strength-density relations of the virgin lattices roughly follow $E/E_0 \propto (\rho/\rho_0)^{2.9}$ and $\sigma_s/\sigma_0 \propto (\rho/\rho_0)^{1.2}$, where E, E_0, σ_s, and σ_0 are Young's modulus of the ceramic lattice, Young's modulus of the solid ceramic (1.39 GPa), flexural strength of the ceramic lattice, and flexural strength of the solid ceramic (18.2 MPa), respectively. Note that the scaling indices here (*i.e.*, 2.9 and 1.2) are higher from the theoretically predicted scaling index (~1) for the stretching-dominant octet truss structures,[45] probably because of the hierarchically porous nature of the employed ceramic lattice structures: bending-dominant in the open porous material and stretching-dominant in the octet architecture (Fig. 4G). After healing, the power index of the stiffness-density law remains as ~3; however, the power index of the strength-density law increases to 4.2. The index increase of the strength-density law is possibly due to the difficulty of bridging the fractured interface for the low-density lattices. We also find that within the existing material property space of ceramic lattice structures, the relative stiffness and strength of the studied virgin ceramic lattices are

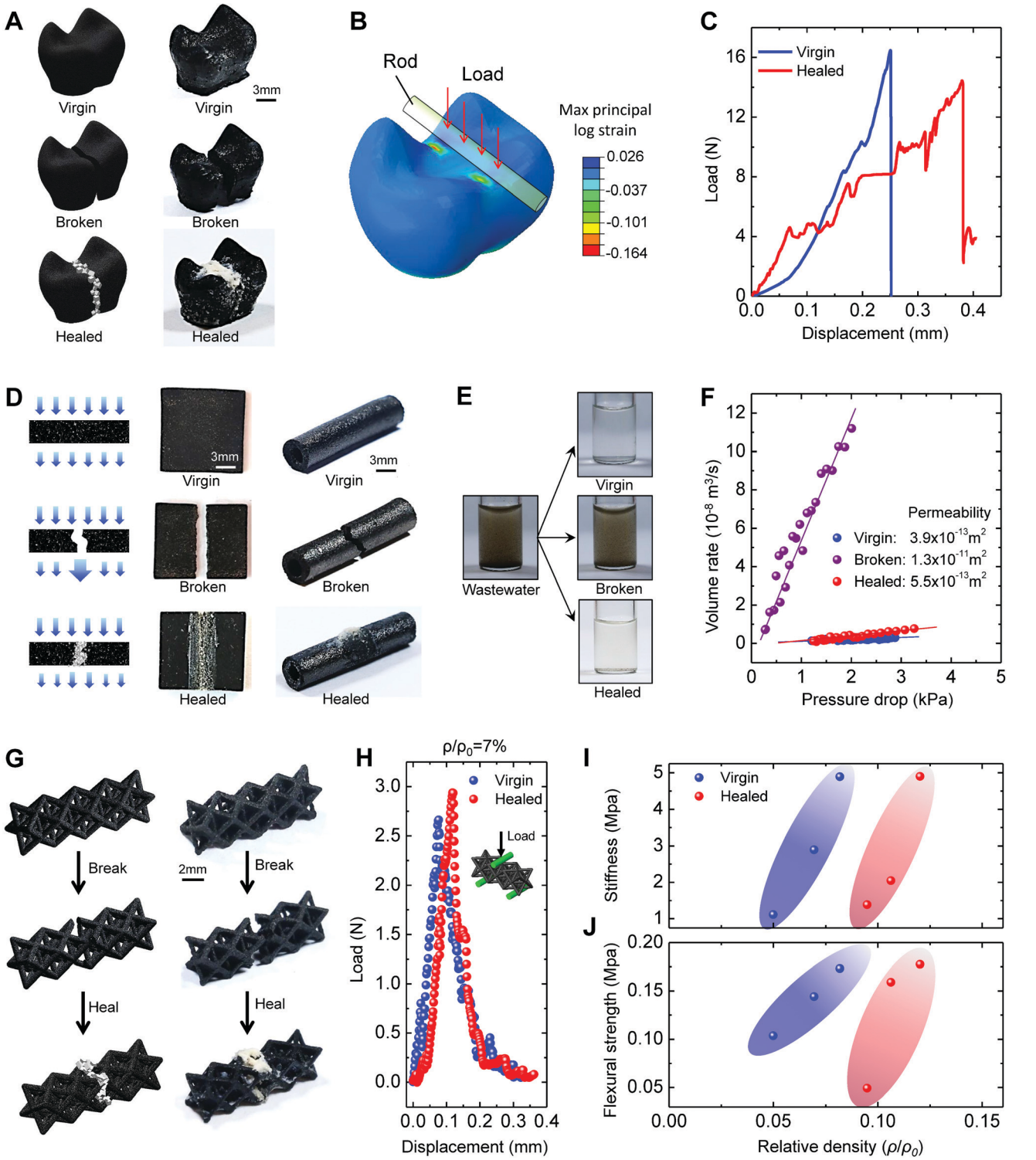

Fig. 4 On-demand healing of 3D-printed ceramic structures. (A) Schematics and samples to show the fracture and healing of a ceramic dental crown. (B) Finite element simulations of the ceramic crowns under a rod-compression load (14.4 N). (C) Load–displacement curves of virgin and healed ceramic crowns under the compression of a transverse rod. (D) Samples and schematics to show fracture and healing of water membranes in flat-sheet and tubular configurations. (E) Feed wastewater and filtrate for the virgin, broken and healed water treatment membranes. (F) Relationships between the filtrate flow rate and pressure drop through the virgin, broken, and healed ceramic water membranes. (G) Schematics and samples to show the fracture and healing of an octet ceramic lattice. (H) Load-displacement curves of virgin and healed ceramic lattices in 3PD tests. The relative density of the lattice is ρ/ρ_0 = 7%, where ρ and ρ_0 are densities of lattice and solid ceramic, respectively. (I) Effective stiffnesses and (J) flexural strengths of virgin and healed lattices as functions of their relative densities ρ/ρ_0.

within a comparable range of other reported ceramic lattices (Fig. S21A and B, ESI†).[3–7] Importantly, the current study opens two new material-property spaces for the stiffness-density and the strength-density of healed ceramic lattices (Fig. S21C and D, ESI†).[46–50] To the best of our knowledge, these are the first material-property Ashby charts for healed ceramic cellular structures (Fig. 4I, J and Fig. S21C and D, ESI†).[49]

Autonomous healing of ceramic armor. Different from the above three examples with the on-demand application of the healing medium, we here show that the paradigm can be used to heal ceramic armor autonomously. Ceramics are commonly used in armored vehicles and ballistic vests because they typically have excellent projectile resistance.[12] Ceramic materials dissipate the kinetic energy of bullets or shrapnel by damaging their structures to diminish the penetration. However, this feature also spawns a limitation of ceramic armor: they may not be reused after a fracture. To address this limitation, we here propose a type of bacteria-assisted autonomously-healable ceramic armor. To demonstrate the concept, we 3D-printed a porous ceramic armor and preloaded with bacteria-saturated growth medium and precipitation medium (Fig. 5A). This pre-treated ceramic armor is assembled on a body model and an

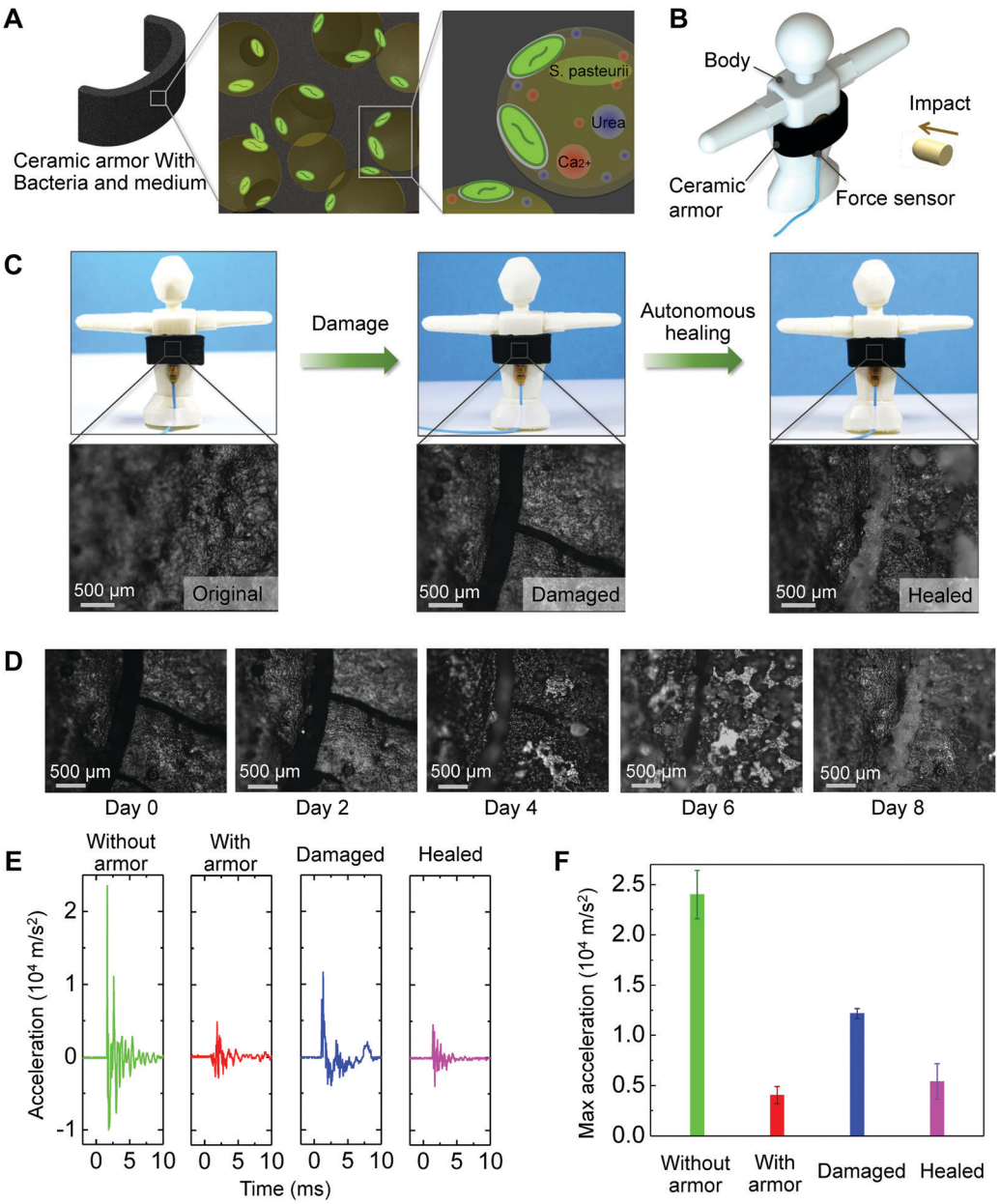

Fig. 5 Autonomous healing of 3D-printed ceramic armor. (A) Schematics of the autonomous healing mechanism. (B) Schematics of the impact experiment. (C) Samples and microscope pictures to show damage and healing of ceramic armor. (D) Microscope pictures to show the autonomous healing process over eight days. (E and F) Acceleration signals and max acceleration for different situations (body with armor, without armor, with damaged armor, and with healed armor). Error bars in (F) represent standard deviations of 3–7 samples.

impact is applied to the armor through a dropping weight (10 g) (Fig. 5B). If the impact force is relatively large, the ceramic armor will be damaged with microcracks (Fig. 5C). These microcracks can be autonomously healed without external interventions: calcite crystals gradually nucleate and grow from day 4, and fully fill the microcracks over 8 days (Fig. 5C and D). To verify the effect of the crack-healing, we carry out impact tests on the ceramic armors with a relatively small impact force. The acceleration signals are collected to estimate the impact force acting on the body model (Fig. 5E). We find that the maximum acceleration of the non-shaded body is around 2.4×10^4 m s^{-2}, and the value is reduced to 0.48×10^4 m s^{-2} after using the virgin ceramic armor (Fig. 5F). When the armor is damaged, a larger acceleration signal (1.2×10^4 m s^{-2}) is acquired, attesting the reduced protection ability of this armor. When the armor is autonomously healed, the measured acceleration reduces to the similar level to that of the virgin armor (0.5×10^4 m s^{-2}). Note that on-demand healing may also be applicable to the armor example; however, we here employ pre-filled bacterial solution to enable autonomous healing without dissembling the structure after a fracture. This autonomous healing may have a limitation that $CaCO_3$ crystals may unselectively nucleate through the whole armor structure. This limitation may be mitigated by judiciously separating the bacteria and precipitation media within the armor structures.[51,52]

Conclusions

In summary, we present a paradigm for healing 3D-printed ceramics at room temperature. The paradigm relies on bacteria-assisted interfacial precipitation of $CaCO_3$ crystals to bridge fracture interfaces of porous ceramics. Unlike high-temperature healing of existing healable bulk ceramics (Table S1, ESI†),[14–21] the healing of 3D-printed ceramics at room temperature may facilitate the possibility of *in situ* or autonomous healing of ceramics with various complex architectures for a wide range of room-temperature applications, such as *in vitro* biomedical devices,[10] water treatment membranes,[11] body armor,[12] and piezoelectric actuators and capacitors.[53] Unlike existing epoxy-glue-enabled ceramic repairing (Table S1, ESI†), the demonstrated method has three outstanding features: (1) the precipitated interface features similar strength as that of virgin ceramics; (2) the precipitated interface can sustain relatively high temperatures (*i.e.*, 650–750 °C); and (3) the precipitation process can occur on any complex interface within the 3D-architected structure. We expect our method to apply not only to polymer-derived ceramics[3,4] but also to other types of 3D-printed ceramics, such as binder-bridged ceramics[1,2,7,54,55] and coated ceramics.[5,6] In addition, this method may be translatable to the healing of various traditionally-unhealable 3D-architected materials, such as 3D-printed glassy polymers,[56] metals,[57] or alloys,[58] given that that the employed material is compatible with the used bacteria such that the bacteria can attach to the material surface to assist the heterogeneous nucleation of the $CaCO_3$ crystals.

Conflicts of interest

The University of Southern California has filed a patent application related to the work described here.

Acknowledgements

The authors acknowledge the funding support from the Air Force Office of Scientific Research (FA9550-18-1-0192) and National Science Foundation (CMMI-1762567). SEM images were obtained in the Core Center of Excellence in Nano Imaging at USC. The authors thank Dr Liming Xiong from Iowa State University for fruitful discussions.

Notes and references

1 A. Zocca, P. Colombo, C. M. Gomes and J. Günster, *J. Am. Ceram. Soc.*, 2015, **98**, 1983–2001.
2 J. W. Halloran, *Annu. Rev. Mater. Res.*, 2016, **46**, 19–40.
3 Z. C. Eckel, C. Zhou, J. H. Martin, A. J. Jacobsen, W. B. Carter and T. A. Schaedler, *Science*, 2016, **351**, 58–62.
4 E. Zanchetta, M. Cattaldo, G. Franchin, M. Schwentenwein, J. Homa, G. Brusatin and P. Colombo, *Adv. Mater.*, 2016, **28**, 370–376.
5 D. Jang, L. R. Meza, F. Greer and J. R. Greer, *Nat. Mater.*, 2013, **12**, 893.
6 L. R. Meza, S. Das and J. R. Greer, *Science*, 2014, **345**, 1322–1326.
7 J. T. Muth, P. G. Dixon, L. Woish, L. J. Gibson and J. A. Lewis, *Proc. Natl. Acad. Sci. U. S. A.*, 2017, **114**, 1832–1837.
8 N. P. Padture, M. Gell and E. H. Jordan, *Science*, 2002, **296**, 280–284.
9 W. Li, J. Liu and D. Zhao, *Nat. Rev. Mater.*, 2016, **1**, 16023.
10 J. Park and R. S. Lakes, *Biomaterials: an introduction*, Springer Science & Business Media, 2007.
11 Z.-X. Low, Y. T. Chua, B. M. Ray, D. Mattia, I. S. Metcalfe and D. A. Patterson, *J. Membr. Sci.*, 2017, **523**, 596–613.
12 P. D. G. Pugh and M. Pugh, *Naval ceramics*, Ceramic Book Co., 1971.
13 B. G. Compton and J. A. Lewis, *Adv. Mater.*, 2014, **26**, 5930–5935.
14 M. Chu, S. Sato, Y. Kobayashi and K. Ando, *Fatigue Fract. Eng. Mater. Struct.*, 1995, **18**, 1019–1029.
15 K. Ando, K. Furusawa, M. C. Chu, T. Hanagata, K. Tuji and S. Sato, *J. Am. Ceram. Soc.*, 2001, **84**, 2073–2078.
16 K. Ando, M.-C. Chu, K. Tsuji, T. Hirasawa, Y. Kobayashi and S. Sato, *J. Eur. Ceram. Soc.*, 2002, **22**, 1313–1319.
17 G. M. Song, Y. T. Pei, W. G. Sloof, S. B. Li, J. T. M. De Hosson and S. van der Zwaag, *Scr. Mater.*, 2008, **58**, 13–16.
18 S. Li, G. Song, K. Kwakernaak, S. van der Zwaag and W. G. Sloof, *J. Eur. Ceram. Soc.*, 2012, **32**, 1813–1820.
19 S. V. Raj, M. Singh and R. T. Bhatt, NASA/TM—2014-218352, 2014.
20 W. G. Sloof, R. Pei, S. A. McDonald, J. L. Fife, L. Shen, L. Boatemaa, A.-S. Farle, K. Yan, X. Zhang, S. van der Zwaag, P. D. Lee and P. J. Withers, *Sci. Rep.*, 2016, **6**, 23040.

21 T. Osada, K. Kamoda, M. Mitome, T. Hara, T. Abe, Y. Tamagawa, W. Nakao and T. Ohmura, *Sci. Rep.*, 2017, **7**, 17853.
22 M. Guan, W. Yao, R. Liu, K. S. Lam, J. Nolta, J. Jia, B. Panganiban, L. Meng, P. Zhou and M. Shahnazari, *Nat. Med.*, 2012, **18**, 456.
23 A. Schindeler, M. M. McDonald, P. Bokko and D. G. Little, *Semin. Cell Dev. Biol.*, 2008, **19**(5), 459–466.
24 D. Taylor, J. G. Hazenberg and T. C. Lee, *Nat. Mater.*, 2007, **6**, 263.
25 H.-P. Wiesmann, M. Hartig, U. Stratmann, U. Meyer and U. Joos, *Biochim. Biophys. Acta, Mol. Cell Res.*, 2001, **1538**, 28–37.
26 K. Van Tittelboom and N. De Belie, *Materials*, 2013, **6**, 2182–2217.
27 V. Achal and A. Mukherjee, *Constr. Build. Mater.*, 2015, **93**, 1224–1235.
28 W. Li, B. Dong, Z. Yang, J. Xu, Q. Chen, H. Li, F. Xing and Z. Jiang, *Adv. Mater.*, 2018, 1705679.
29 W. De Muynck, N. De Belie and W. Verstraete, *Ecol. Eng.*, 2010, **36**, 118–136.
30 H. M. Son, H. Y. Kim, S. M. Park and H. K. Lee, *Materials*, 2018, **11**, 782.
31 M. B. Schaffler and D. B. Burr, *J. Biomech.*, 1988, **21**, 13–16.
32 J.-Y. Rho, L. Kuhn-Spearing and P. Zioupos, *Med. Eng. Phys.*, 1998, **20**, 92–102.
33 L. J. Gibson, *J. Biomech.*, 1985, **18**, 317–328.
34 B. Li and R. M. Aspden, *J. Bone Miner. Res.*, 1997, **12**, 641–651.
35 J. Fischgrund, D. Paley and C. Suter, *Clin. Orthop. Relat. Res.*, 1994, 31–37.
36 Y. H. An and R. J. Friedman, *J. Biomed. Mater. Res.*, 1998, **43**, 338–348.
37 Y. Zahra, F. Djouani, B. Fayolle, M. Kuntz and J. Verdu, *Prog. Org. Coat.*, 2014, **77**, 380–387.
38 A. Amaro, P. Reis, M. Neto and C. Louro, *J. Reinf. Plast. Compos.*, 2013, **32**, 1018–1029.
39 D. A. Porter, K. E. Easterling and M. Sherif, *Phase Transformations in Metals and Alloys, (Revised Reprint)*, CRC Press, 2009.
40 C. Zener, *J. Appl. Phys.*, 1949, **20**, 950–953.
41 Q. Wang, J. A. Jackson, Q. Ge, J. B. Hopkins, C. M. Spadaccini and N. X. Fang, *Phys. Rev. Lett.*, 2016, **117**, 175901.
42 J. R. Kelly, *Dent. Clin.*, 2004, **48**, 513–530.
43 C. Minas, D. Carnelli, E. Tervoort and A. R. Studart, *Adv. Mater.*, 2016, **28**, 9993–9999.
44 X. Zheng, H. Lee, T. H. Weisgraber, M. Shusteff, J. DeOtte, E. B. Duoss, J. D. Kuntz, M. M. Biener, Q. Ge, J. A. Jackson, S. O. Kucheyev, N. X. Fang and C. M. Spadaccini, *Science*, 2014, **344**, 1373–1377.
45 V. S. Deshpande, N. A. Fleck and M. F. Ashby, *J. Mech. Phys. Solids*, 2001, **49**, 1747–1769.
46 T. A. Schaedler and W. B. Carter, *Annu. Rev. Mater. Res.*, 2016, **46**, 187–210.
47 N. Fleck, V. Deshpande and M. Ashby, *Proc. R. Soc. London, Ser. A*, 2010, **466**, 2495–2516.
48 L. Montemayor, V. Chernow and J. R. Greer, *MRS Bull.*, 2015, **40**, 1122–1129.
49 L. J. Gibson and M. F. Ashby, *Cellular solids: structure and properties*, Cambridge University Press, 1999.
50 H. N. Wadley, *Philos. Trans. R. Soc., A*, 2006, **364**, 31–68.
51 K. S. Toohey, N. R. Sottos, J. A. Lewis, J. S. Moore and S. R. White, *Nat. Mater.*, 2007, **6**, 581.
52 S. R. White, N. R. Sottos, P. H. Geubelle, J. S. Moore, M. R. Kessler, S. Sriram, E. Brown and S. Viswanathan, *Nature*, 2001, **409**, 794.
53 B. Jaffe, *Piezoelectric ceramics*, Elsevier, 2012.
54 F. Kotz, K. Arnold, W. Bauer, D. Schild, N. Keller, K. Sachsenheimer, T. M. Nargang, C. Richter, D. Helmer and B. E. Rapp, *Nature*, 2017, **544**, 337.
55 Y. Yang, Z. Chen, X. Song, B. Zhu, T. Hsiai, P.-I. Wu, R. Xiong, J. Shi, Y. Chen and Q. Zhou, *Nano Energy*, 2016, **22**, 414–421.
56 M. Hegde, V. Meenakshisundaram, N. Chartrain, S. Sekhar, D. Tafti, C. B. Williams and T. E. Long, *Adv. Mater.*, 2017, **29**, 1701240.
57 A. Vyatskikh, S. Delalande, A. Kudo, X. Zhang, C. M. Portela and J. R. Greer, *Nat. Commun.*, 2018, **9**, 593.
58 J. H. Martin, B. D. Yahata, J. M. Hundley, J. A. Mayer, T. A. Schaedler and T. M. Pollock, *Nature*, 2017, **549**, 365.